steel research international
www.steel-research.de

Modeling Asymmetric Flow in the Thin-Slab Casting Mold Under Electromagnetic Brake

Alexander Vakhrushev, Abdellah Kharicha, Ebrahim Karimi-Sibaki, Menghuai Wu, Andreas Ludwig, Gerald Nitzl, Yong Tang, Gernot Hackl, and Josef Watzinger*

Continuous casting (CC) is nowadays the world-leading technology for steel production. The thin slab casting (TSC) is featured by a slab shape close to the final products and a high casting speed. The quality of the thin slabs strongly depends on the uniformity of the turbulent flow and the superheat distribution, defining the solid shell growth against a funnel-shaped mold. In most studies, it is commonly assumed that the submerged entry nozzle (SEN) is properly arranged, and the melt inflow is symmetric. However, the misalignment or clogging of the nozzle can lead to an asymmetric flow pattern. Herein, the asymmetry is imposed via a partial SEN clogging: a) a local porous zone inside the nozzle reflects the presence of the clog material; b) the resistance of the clog is varied from low to high values. The solidification during TSC is modeled, including the effects of the turbulent flow. The variation of the flow pattern and the solidified shell thickness are studied for different permeability values of the SEN clogging. These effects are considered with and without the applied electromagnetic brake (EMBr) using an in-house magnetohydrodynamics (MHD) and solidification solver developed within the open-source package OpenFOAM.

A. Vakhrushev, A. Kharicha, E. Karimi-Sibaki
Christian Doppler Laboratory for Metallurgical Applications of Magnetohydrodynamics
Montanuniversität Leoben
Franz-Josef Str. 18, A-8700 Leoben, Austria
E-mail: abdellah.kharicha@unileoben.ac.at

M. Wu, A. Ludwig
Chair of Simulation and Modelling of Metallurgical Processes
Department of Metallurgy
Montanuniversität Leoben
Franz-Josef Str. 18, A-8700 Leoben, Austria

G. Nitzl
RHI Magnesita GmbH
Kranichberggasse 6, A-1120 Vienna, Austria

Y. Tang, G. Hackl
RHI Magnesita GmbH
Technology Centre, Magnesitstrasse 2, A-8700 Leoben, Austria

J. Watzinger
Primetals Technologies
Turmstrasse 44, A-4031 Linz, Austria

The ORCID identification number(s) for the author(s) of this article can be found under https://doi.org/10.1002/srin.202200088.

DOI: 10.1002/srin.202200088

1. Introduction

Industrial thin-slab casting (TSC) of the steel became nowadays important and effective continuous casting technology since its start in the year 1989.[1] It is featured by a slab size close to the final product shape, uniformity of the mechanical properties, reduced central macrosegregation, high casting speed, and application in the direct rolling concept. Energy savings of more than 40% in comparison to conventional thick casting are vital for the steel industry. However, a highly turbulent flow develops during the steel feeding via a submerged entry nozzle (SEN) into a narrow (typically funnel-shaped) thin-slab mold.

A wide number of detailed reviews on the multiphase phenomena happening in the continuous casting mold were published within recent years.[2–6] One of critical issues during continuous casting (CC) is related to the melt flow instability, its asymmetry and general violation of the desired flow pattern, which can originate for example from the partial SEN clogging. Very recently, Barati et al. discussed the mechanisms of the clog deposition on the refractory walls as well as the modeling techniques and the possible role of the melt solidification inside the clogging material.[7–10] Vakhrushev et al. disclosed that the damage of the protective fiber layer can promote a parasitic solidification inside the SEN bore, causing meniscus acceleration and sink of the superheat of the fresh melt; such a scenario is further worsened by the associated growth of the clog material strengthened by the solidification of the entrapped melt.[11]

The asymmetric flow in the mold was investigated experimentally in early 1990 s by Gupta and Lahiri and later on supplemented by the consequent works of other researchers.[12–19]

The interaction of the fresh hot melt turbulent flow with the solidifying solid shell is generally an important topic in the solidification process. It becomes especially crucial in continuous casting.[20] Since it causes the local remelting of the solidifying shell, its further enhancement at the jet impingement area due to the flow asymmetry can lead to breakouts below the mold exit. Applying a flow control technique in the mold is favorable. The electromagnetic brake (EMBr) is one of the well-known and widely applied technologies in the continuous casting of steel.[21] It allows reducing the impingement effect of the hot jets, promotes the calmness of the meniscus, and enhances the superheat transport for stable flux melting rate, etc.[22] A recent study of the EMBr effect on the non-metallic inclusions removal was done by Yin et al.[23] An advance technique, combining a mold EMBr and a strand electromagnetic stirring (SEMS) to enhance uniformity of the solidification, was presented by Wang et al.[24] Another new approach, introducing two vertical magnetic poles (VMPs) in a freestanding and adjustable EMBr (FAC-EMBr) to weaken the jets interference with the shell and meniscus region, was proposed by Li et al.[25]

Nowadays, the advance numerical modeling technique resulted in the numerous studies on this topic.[24,26–29] In the presented study, the coupled solidification and magnetohydrodynamics (MHD) models, previously developed and verified by the current authors,[30–33] implemented in the open-source computational fluid dynamics (CFD) package OpenFOAM,[34] are applied to simulate the effects of the electromagnetic braking on the asymmetric melt flow caused by the partial SEN clogging.

The influence on the solid shell profile is newly studied in very details for different permeabilities of the clog material without and with the applied magnetic field, revealing the effects of the acting MHD forces.

2. Numerical Model

In the current work, a constant density is assumed for the solidifying melt. Thus, the flow in the continuous casting mold, including magnetohydrodynamic effects, can be described as a set of Navier–Stokes equations for the incompressible fluid. The corresponding mass and momentum conservation equations are

$$\nabla \cdot \vec{\boldsymbol{u}} = 0 \tag{1}$$

$$\rho\left(\tfrac{\partial \vec{\boldsymbol{u}}}{\partial t} + \nabla \cdot (\vec{\boldsymbol{u}} \otimes \vec{\boldsymbol{u}})\right) = -\vec{\nabla} p + \nabla \cdot (\mu[\nabla \vec{\boldsymbol{u}} + \nabla^{\mathrm{T}} \vec{\boldsymbol{u}}]) - \nabla \cdot \boldsymbol{\tau}_{\mathrm{sgs}} + \vec{\boldsymbol{F}}_{\mathrm{Darcy}} + \vec{\boldsymbol{F}}_{\mathrm{clog}} + \vec{\boldsymbol{F}}_{\mathrm{L}} \tag{2}$$

with the velocity $\vec{\boldsymbol{u}}$, melt density ρ, dynamic viscosity μ, and the pressure field p characterizing the fluid flow. In the current study, the turbulent effects are modeled by large-eddy simulation (LES) method. The turbulent viscous stress tensor $\boldsymbol{\tau}_{\mathrm{sgs}}$ is simulated on the sub-grid level using Wall-Adapting Local Eddy-viscosity (WALE) model.[35] The drag force $\vec{\boldsymbol{F}}_{\mathrm{Darcy}}$ defines the interaction between the dendritic mushy zone and the liquid melt. To model the SEN clogging, an additional term $\vec{\boldsymbol{F}}_{\mathrm{clog}} = -\mu D \vec{\boldsymbol{u}}$ is introduced, where D is the porous resistance of the clog material. The Lorentz force $\vec{\boldsymbol{F}}_{\mathrm{L}}$ is included in momentum Equation (2) as following

$$\vec{\boldsymbol{F}}_{\mathrm{L}} = \vec{\boldsymbol{j}} \times \vec{\boldsymbol{B}}_0 \tag{3}$$

The electric potential method is applied being valid at low magnetic Reynolds numbers,[36] at which the electric field $\vec{\boldsymbol{E}}$ becomes curl-free $\nabla \cdot \vec{\boldsymbol{E}} \equiv \vec{o}$ and the electric potential φ can be introduced as $\vec{\boldsymbol{E}} = -\vec{\nabla}\varphi$. The electric current from the Ohm's law becomes

$$\vec{\boldsymbol{j}} = \sigma(-\vec{\nabla}\varphi + \vec{\boldsymbol{u}} \times \vec{\boldsymbol{B}}_0) \tag{4}$$

where the parameter σ is the electrical conductivity. The electric potential φ is calculated by solving the corresponding Poisson equation.

$$\nabla \cdot (\sigma \vec{\nabla} \varphi) = \nabla \cdot (\sigma(\vec{\boldsymbol{u}} \times \vec{\boldsymbol{B}}_0)) \tag{5}$$

Electric conductivity σ is considered to vary 1.5 times between liquid melt and solidified shell. The correct prediction of the latent heat advection is crucial for the growth of the solid shell.[20,30] The corresponding energy equation is solved for the temperature field T in its general advection–diffusion form as

$$\rho C_{\mathrm{p}}\left[\frac{\partial T}{\partial t} + \nabla \cdot (\vec{\boldsymbol{u}} T)\right] = \nabla \cdot (\lambda \nabla T) + \rho L\left[\frac{\partial f_{\mathrm{s}}}{\partial t} + \nabla \cdot (f_{\mathrm{s}} \vec{\boldsymbol{u}}_{\mathrm{s}})\right] \tag{6}$$

with specific heat C_{p}, thermal conductivity λ, latent heat of fusion L, and corresponding solid fraction f_{s}. The solid velocities $\vec{\boldsymbol{u}}_{\mathrm{s}}$ are estimated using the linear elasticity model for the shell by applying the elastostatics condition to obtain the Navier–Cauchy equation.[37,38]

$$(\Lambda + M)\nabla(\nabla \cdot \vec{\boldsymbol{\delta}}) + M(\nabla \cdot \nabla \vec{\boldsymbol{\delta}}) = 0 \tag{7}$$

where Λ and M are Lamé parameters, and the displacement vector $\vec{\boldsymbol{\delta}}$ meets $\vec{\boldsymbol{u}}_{\mathrm{s}} = \partial \vec{\boldsymbol{\delta}}/\partial t$. By transforming Equation (7) from Lagrangian into Eulerian frame of reference, the obtained Laplace equations $\nabla \cdot \nabla \vec{\boldsymbol{u}}_{\mathrm{s}} = 0$ is solved using corresponding boundary condition[30,39]

$$\vec{\boldsymbol{u}}_{\mathrm{s}}^{\mathrm{mold}} = U_{\mathrm{cast}}(\vec{\boldsymbol{e}}_{\mathrm{y}} - \langle \vec{\boldsymbol{e}}_{\mathrm{y}}, \vec{\boldsymbol{n}} \rangle \vec{\boldsymbol{n}})/||\vec{\boldsymbol{e}}_{\mathrm{y}} - \langle \vec{\boldsymbol{e}}_{\mathrm{y}}, \vec{\boldsymbol{n}} \rangle \vec{\boldsymbol{n}}|| \tag{8}$$

where U_{cast} is the strand's casting speed; $\vec{\boldsymbol{e}}_{\mathrm{y}}$ and $\vec{\boldsymbol{n}}$ are the unit vectors in the casting direction and normal to the funnel-shaped mold surface as sketched in **Figure 1**. Recently, the authors presented an advanced viscoplastic approach to model a withdrawal of the solidifying shell in the curved TSC mold, which is an essential topic for the future studies.[40]

Based on the simulated temperature and the solid/liquid phases distribution, a corresponding source term in the momentum equation, Equation (2), is estimated.

$$\vec{\boldsymbol{F}}_{\mathrm{Darcy}} = -\frac{\mu}{K}(\vec{\boldsymbol{u}} - \vec{\boldsymbol{u}}_{\mathrm{s}}) \ \text{ with } K = f_l^3/f_s^2 \cdot 6 \times 10^{-4} \cdot \mathrm{PDAS}^2 \tag{9}$$

where PDAS stands for the primary dendrite arm spacing, which is calculated using an external thermodynamic–kinetic software package IDS for the modeled steel grade.[41]

For the details of the implementation and verification of the solidification model please, refer to work by Vakhrushev et al.[30]

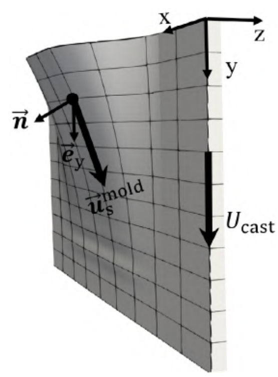

Figure 1. Funnel-shaped mold schematics used to calculate the surface solid velocities $\vec{\boldsymbol{u}}_{\mathrm{s}}^{\mathrm{mold}}$.

According to the developed numerical model described in Equation (1)–(9), a corresponding solver including fluid flow, action of the Lorentz force and considering the solidification, was developed in the open-source CFD package OpenFOAM.[34] The MHD model was previously verified by comparing the modeling results with the experimental measurements presented by Thomas et al.[42]

3. Results and Discussion

The simulation domain and corresponding boundary conditions are displayed in **Figure 2**. The general layout, combining a thin-slab-type SEN, the funnel-shaped CC mold, and the slab's secondary cooling zone, is presented in Figure 2a. An additional asymmetric flow scenario is determined by a clogged region indicated in Figure 2b.

Velocity component, normal to the outlet, is set to the casting speed of 5.5 m min^{-1} (Figure 2a, bottom), preventing the divergence of the numerical simulation due to the backflow development. Simultaneously, a free-slip condition, applied in the transversal direction, allows the flow fluctuations and vortices to travel across the outlet. The fresh melt throughput at the SEN inlet (Figure 2a, top) corresponds to the withdrawal speed at the slab region by satisfying the mass conservation during a coupled simulation. A superheated (by 28 °C) alloy is fed through the SEN port. At the outlet, a free stream condition is applied for the temperature field. The cooling conditions consist of the heat-flux profile at the TSC mold region (Figure 2c), and include the convective heat transfer along the strand surface (Figure 2a). The semiempirical heat-flux distribution depends on the casting speed. An averaged heat-transfer coefficient $HTC = 1100$ W m^{-2} K is assumed for the strand part. The HTC value was recovered based on the experimental measurements by solving the inverse heat conduction problem (IHCP).[43]

The melt solidification is defined by the temperature-dependent solid fraction curve (Figure 2d), calculated using IDS software based on the alloy composition.[41] The arrangement of the local electromagnetic braking and the applied magnetic field magnitude are detailed in Figure 2e. The detailed alloy properties and casting conditions are summarized in **Table 1**.

As mentioned earlier, calculation of the solid velocities distribution plays important role for the correct prediction of the latent heat advection. The exclusion of the $\rho L \nabla \cdot (f_s \vec{u}_s)$ term from Equation (6) results in overprediction of the solid shell thickness by 60–90%.[30] The calculated solid velocities are presented in **Figure 3** for the funnel part of the 1100 mm high TSC mold. The surface components u_s^x and u_s^z in the transversal and thickness directions are illustrated in Figure 3a. Notice that the vertical component u_s^y equals to the casting speed U_{cast}. Distribution of the solid velocity magnitude $|\vec{u}_s|$ through the solid shell thickness is detailed in Figure 3b. The geometry is shrunk four times in transversal and casting directions in Figure 3b to make the $|\vec{u}_s|$ field more visible inside the thin solid shell.

The instantaneous velocity field distribution, simulated using an early described solidification model, is shown in **Figure 4**. The melt flow pattern is compared for the cases without magnetic field (Figure 4a) and with the applied electromagnetic braking (Figure 4b).

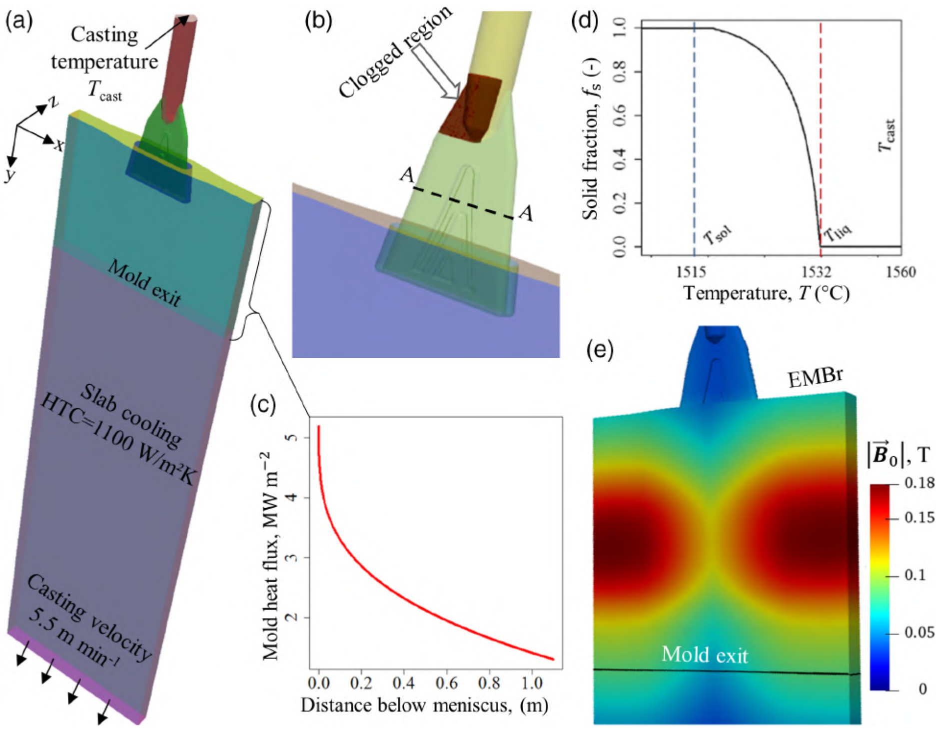

Figure 2. Numerical simulation setup: a) thin-slab submerged entry nozzle (SEN) and mold geometry with the defined boundary conditions; b) location of the modeled clogged region; c) mold heat-flux distribution; d) solidification curve; and e) distribution of the applied electromagnetic brake (EMBr) magnetic field.

Table 1. Material properties and casting conditions.

Property	Unit	Quantity
ρ	$\mathrm{kg\,m^{-3}}$	7850
C_p	$\mathrm{J\,kg^{-1}\,K^{-1}}$	838.2
λ	$\mathrm{W\,m^{-1}\,K^{-1}}$	35
μ	Pa s	0.0061
L	$\mathrm{J\,kg^{-1}}$	243000
σ	$\mathrm{S\,m^{-1}}$	770 000[a) $\approx$ 981750[b)
U_{cast}	$\mathrm{m\,min^{-1}}$	5.5
T_{cast}	°C	1560
T_{liq}	°C	1532
T_{sol}	°C	1515

[a)] $T = 1526.85$°C; [b)] $T = 526.85$°C.

As it was very recently elucidated by the authors, the topology of the Lorentz force action on the submerged jet is very complex: it causes braking and flattening of the jet's core; simultaneously, the liquid from the bulk is accelerated and entrained due to the closure of the induced electric current lines.[44] That results in a formation of two reverse flow zones above and beneath the jets fed from the ports of the CC SEN; with growing EMBr power, they can initiate the opposite flow in the upper part of the CC mold.[33] One can see in Figure 4b that the jets become more stable, and the turbulent structures are significantly damped at the magnetic field presence. The critical areas with the meniscus flow velocity $|\vec{u}| > 0.4\,\mathrm{m\,s^{-1}}$ promoting the slag entrapment risks are dramatically suppressed by applying the EMBr.

The turbulent jet flow inside the TSC mold has dramatic effect on the heat transfer and solidification. The distribution of the temperature field for the flow without magnetic field and with the applied EMBr is compared in **Figure 5**.

It should be mentioned that a full coupling between the turbulent flow, solidification, and the MHD force is performed. The values in Figure 5 are scaled between the liquidus and the casting temperature (see Figure 2d) to clearly indicate the amount of the superheat transported through the simulation domain. For the case without magnetic field in Figure 5a, the hot jets tend to go down deeper into liquid pool mostly along the narrow walls; the oscillations of higher frequency for the small structures and of lower frequency for the main jets are observed (Figure 4a) leading to the asymmetric superheat transport to the top surface. That can affect the flux melting and liquid slag infiltration being especially important for the quality and sustainable casting process. The meniscus temperature in Figure 5a is just several degrees higher than liquidus, which can cause a frozen meniscus issue.

However, when the electromagnetic braking is applied (Figure 5b), more superheat is maintained by the Lorentz force action at the upper region of the mold. More details of this phenomenon are elucidated in the later discussions.

Next, the melt flow and the solidification were investigated considering the presence of the clogged region (as marked in Figure 2b). The comparison was made for the cases without and with the applied magnetic field and by varying the clogged region porous resistance D.

The flow rate distribution inside the SEN bore for different scenarios is shown in **Figure 6**, which correspond to a Section A-A in Figure 2b located 100 mm above meniscus. The case of the clog-free SEN (Figure 6a) is compared to the additional studies where the clog material resistance D is varied between a low value of $10^6\,\mathrm{m^{-2}}$ (Figure 6b), intermediate one of $10^7\,\mathrm{m^{-2}}$ (Figure 6c) up to a completely one-side-blocked SEN ($D = 10^8\,\mathrm{m^{-2}}$ in Figure 6d).

The quantitative comparison of the flow rates between the clogged and "free" SEN side is provided in Figure 6e. It should be noted that a slight deviation from a perfect 50% balance for the first case is related to the mesh asymmetry generated for a real computer-aided design drawing. For the weakly blocked SEN (Figure 6b), the difference is 2.7% only, while for the case in Figure 6c, it is worsened to almost 15% of misbalance in the flow. The last case in Figure 6d demonstrates up to 92% of the melt going through the non-clogged region of the SEN bore.

It was observed that the flow profiles inside the SEN channel 100 mm above meniscus are not affected by the presence of the

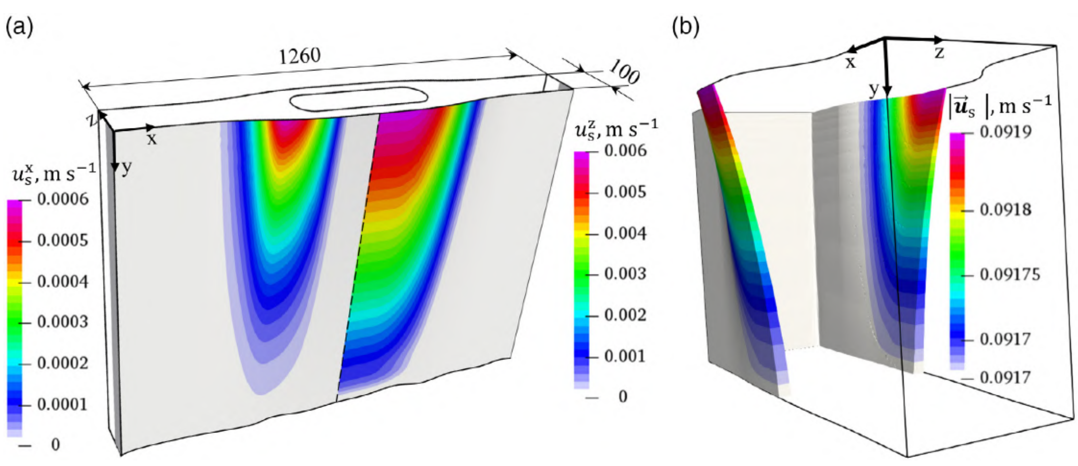

Figure 3. Distribution of the solid velocity $\vec{u}_s$ in the funnel part of the thin-slab casting (TSC) mold: a) components u_s^x and u_s^z along the transversal and thickness directions; b) solid velocity magnitude $|\vec{u}_s|$ inside the solid shell (domain is shrunk by factor of 4 in x and y directions).

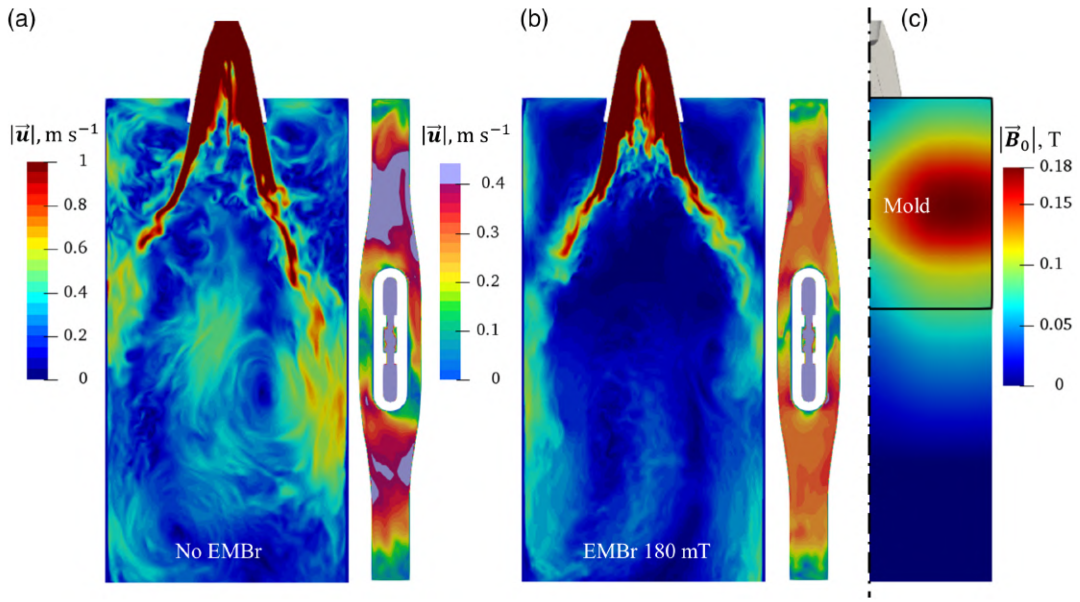

Figure 4. Flow simulation results without clogging: velocity magnitude $|\vec{u}|$ in the mid-plane (left) and at the meniscus level (right) for the cases a) without and b) with the applied EMBr of 180 mT; c) positioning and intensity of the applied magnetic field magnitude $|\vec{B}_0|$. Gray areas mark the critical for the slag entrapment regions with $|\vec{u}| > 0.4\,\mathrm{m\,s^{-1}}$ at the meniscus.

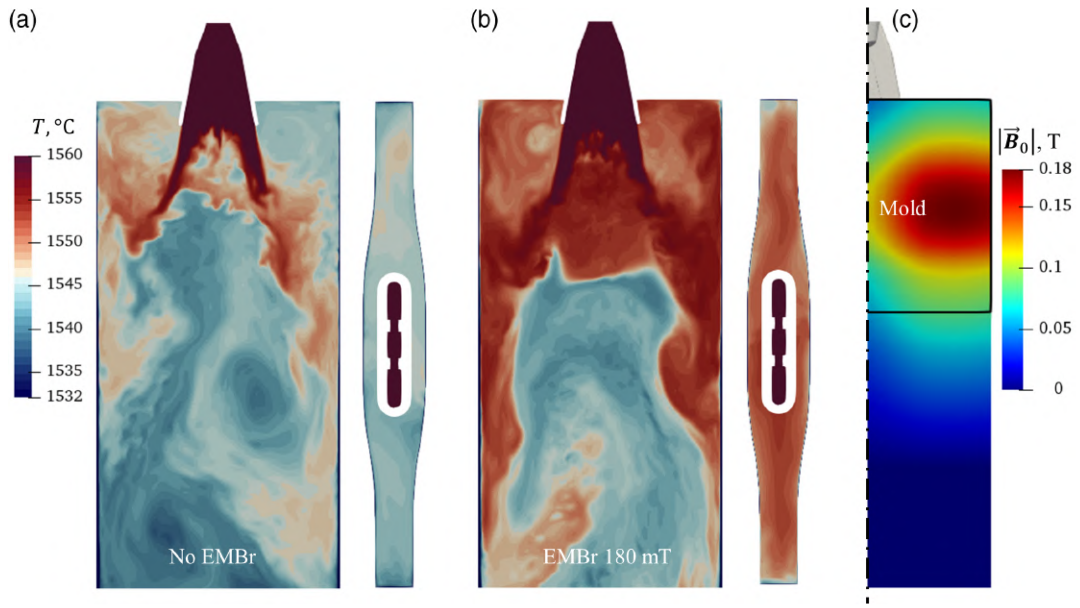

Figure 5. Heat-transfer simulation results without clogging: temperature in the mid-plane (left) and at the meniscus level (right) for the cases a) without and b) with the applied EMBr of 180 mT; c) positioning and intensity of the applied magnetic field magnitude $|\vec{B}_0|$.

EMBr. Moreover, the SEN port outlet velocity was found weakly affected by the applied magnetic field. Our explanation is that the convective flow is too strong before leaving the SEN and the magnetic field strongly decays closer to the meniscus (see Figure 2e). Thereby, the corresponding comparison of the SEN flow with and without the applied magnetic field is not presented for the discussion here.

Next, the corresponding changes of the flow and superheat distribution inside the mold and strand parts are presented and discussed. Hereinafter, a reference value of the porous resistance $D = 10^7\,\mathrm{m^{-2}}$ (see Figure 6c) was selected to analyze the influence of the clogging. Based on the series of numerical studies, a significant flow distortion happens at this specific value, while still allowing the melt to penetrate through the porous region inside the SEN.

As was found during a detailed study presented in **Figure 7**, an asymmetric flow pattern, caused by the clogging formation inside the SEN bore, is completely undesired. The instantaneous

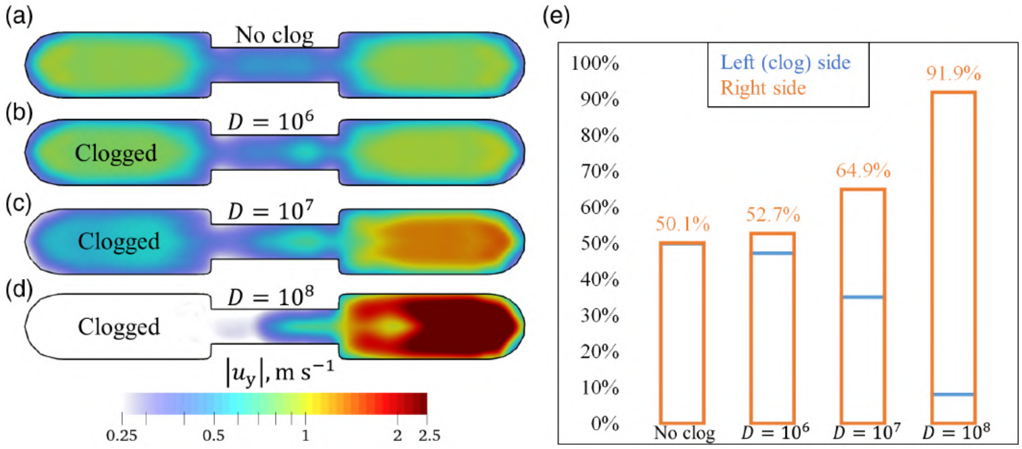

Figure 6. Time-averaged stream-wise velocity $|u_y|$ inside the SEN bore 100 mm above meniscus (Section A-A in Figure 2b): a) SEN free of clog; cases with clogging with the variation of porous resistance b) $D = 10^6\,m^{-2}$; c) $D = 10^7\,m^{-2}$; d) $D = 10^8\,m^{-2}$. e) Summary diagram of the flow rate asymmetry.

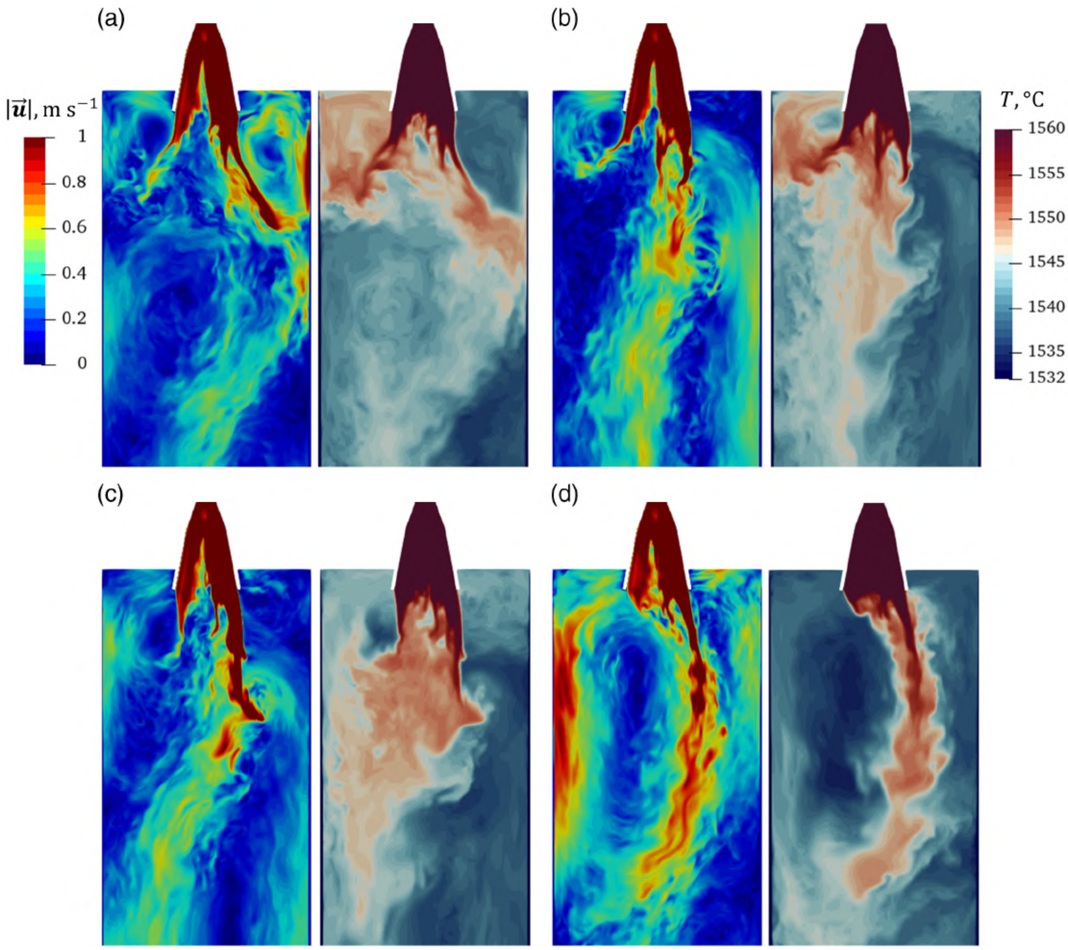

Figure 7. Snapshots of the instantaneous velocity $|\vec{u}|$ (left figures) and temperature T field (right figures) in the midplane capturing the flow instabilities and low superheat regions due to the presence of the clogging inside the SEN bore (case with $D = 10^7\,m^{-2}$ in Figure 6d): a) quasisymmetric flow with cold meniscus on the clogged side; b) asymmetric flow and temperature fields; c) asymmetric flow with the temperatures in a mild range; d) a transition regime with extremely cold meniscus.

velocity field simulated together with the heat transfer clearly displays the formation of the instabilities. The flow alternates between a visually symmetric (Figure 7a) and extremely disproportional patterns (Figure 7b–d). The submeniscus region inside the mold on the "free" side of the SEN becomes dominantly colder since most of the superheat is brought downstream by the faster jet. The left part of the mold on the clogged SEN side is mostly provided with the superheated melt as in Figure 7a,b or

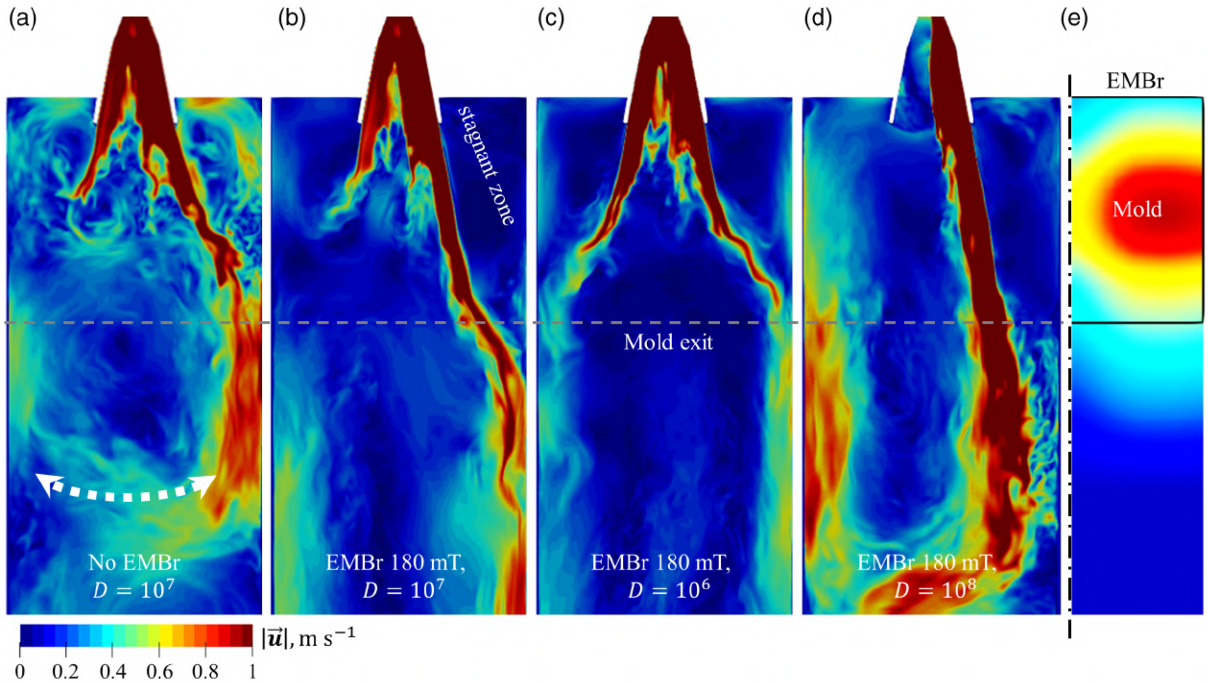

Figure 8. Distribution of the velocity magnitude $|\vec{u}|$ in the midplane of the domain, SEN clogging included a) no magnetic field, $D = 10^7$ m^{-2}; cases with the applied EMBr of 180 mT: b) $D = 10^7$ m^{-2}; c) $D = 10^6$ m^{-2}; d) $D = 10^8$ m^{-2}; e) schematics of the EMBr arrangement.

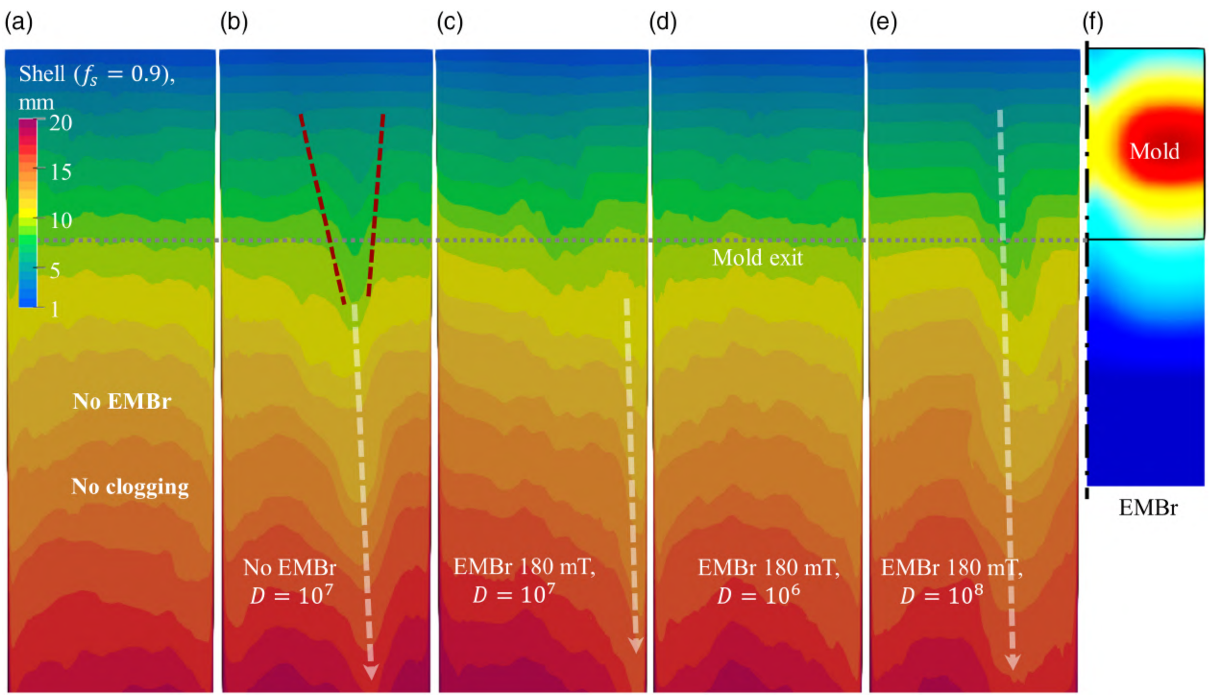

Figure 9. Simulated shell thickness (solid phase $f_s = 0.9$). Cases without EMBr: a) excluding and b) considering SEN clogging. Cases with the applied EMBr (180 mT) with the variation of the clog resistance: c) $D = 10^7$ m^{-2}; d) $D = 10^6$ m^{-2}; e) $D = 10^8$ m^{-2}; f) EMBr schematics.

is at the "mild" temperatures range together with the right side as in Figure 7c. However, in a transition regime of the jet side-to-side swinging (see Figure 7 d), the whole meniscus dangerously drops to the liquidus.

Next, the results for the different permeability cases including EMBr effect are displayed in **Figure 8**. Clogged case with $D = 10^7\,\mathrm{m}^{-2}$, ignoring the EMBr, is shown in Figure 8a for the comparison with more details already presented in Figure 7. Once the magnetic field of 180 mT is applied (Figure 8b), the jets fluctuations are significantly damped. Thereby, the non-clogged side jet penetrates deeper into the liquid pull, and a corresponding sub-meniscus region becomes very calm (see the marked stagnant zone in Figure 8b). For the significantly low resistance $D = 10^6\,\mathrm{m}^{-2}$, no dramatic flow asymmetry was detected (Figure 8c). However, at the high porous resistance level of the clogging material $D = 10^8\,\mathrm{m}^{-2}$, the flow on the clogged side of the SEN was completely blocked, and a strong downward jet was clearly observed.

According to the research, the corresponding changes of the melt flow directly influence the solidified shell thickness. The simulation results of the solidification considering the presence of the clogged SEN region are detailed in **Figure 9**. The solid shell distribution for the case without clogging and without an applied magnetic field is presented in Figure 9a. This simulation is used as a reference for further comparison.

First, when the flow becomes asymmetric (Figure 9b, no EMBr, $D = 10^7\,\mathrm{m}^{-2}$), the stronger throughput on the non-clogged side along with the turbulent jet swinging causes remelting of the solid shell at around one third of the mold width from the narrow face. When the EMBr with the intensity of 180 mT is applied (Figure 9c), the shell remelting site shifts toward the narrow face due to the stabilization of the jet. Next, when the clog

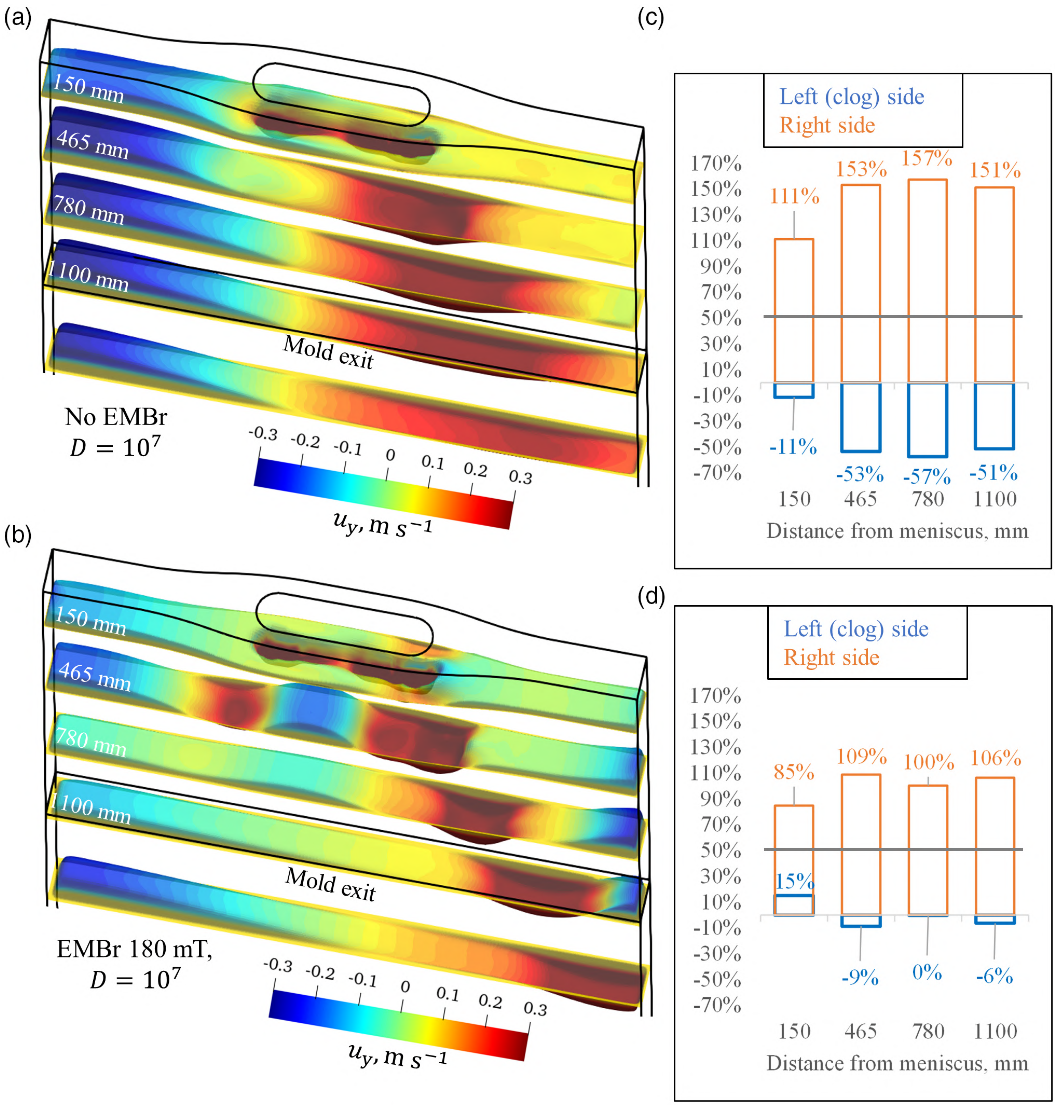

Figure 10. Time-averaged stream-wise velocity u_y: case a) without and b) with the applied magnetic field. Integral flowrate ratio in the mold sections: c) without and d) with EMBr.

resistance D is varied, for the low value ($D = 10^6\ \mathrm{m}^{-2}$), no significant shell remelting is observed (Figure 9d). As expected, for the high porous resistance ($D = 10^8\ \mathrm{m}^{-2}$), the pronounced thinning of the shell is detected parallel to the casting direction due to the strong downward jet (see Figure 8d and 9e).

Next, to summarize the presented study, the influence of the applied EMBr on the flow pattern and on the superheat distribution is detailed for the reference case with $D = 10^7\ \mathrm{m}^{-2}$.

Time-averaged flowrate statistics is presented in **Figure 10**. The horizontal cut-planes are located at 150 (SEN port level), 465, 780, and 1100 mm (corresponding to the mold exit) below the meniscus level. The iso-surfaces in Figure 10a,b are wrapped around by the stream-wise velocity u_y. The logarithmic scaling of the absolute values of u_y was applied to improve the down- and upstream flow comparison by revealing their features.

In case without the EMBr (Figure 10a), a broad area of the downflow on the right (clog-free) side of the mold is detected, which is compensated with the pronounced upflow on the left.

If the magnetic field is applied (Figure 10b), the downstream jet on the right side becomes narrower, the upper roll is reestablished in comparison to Figure 10a. On the left side, a smaller jet is detected departing from the port SEN outlet down-to-the-half-mold depth, which is absent in Figure 10a, and the corresponding upper roll is formed. A minor upward flow is observed in the lower section of the left side of the TSC mold.

An integral flowrate was calculated for the quantitative comparison between the left (clogged) and the right (clog-free) mold sides (see Figure 10c,d). It is based on the surface integral of u_y scaled by the initial net casting speed. Thereby, all values exceeding 100% indicate a relative downward acceleration in this region, whereas the negative flowrates correspond to the areas of the dominant upward flow. The case of a fully symmetric flow would correspond to the positive 50% on both sides of the mold, marked in Figure 10c,d by a horizontal gray line.

Without magnetic field, a strong downflow, reaching 157% of the nominal casting rate, is compensated by the corresponding upward melt motion (the section at 780 mm in Figure 10c).

In comparison to the results in Figure 10c, the improvements are observed in Figure 10d due to the Lorentz force action: the flow toward the meniscus and the disproportion between the left and right sides of the mold are dramatically suppressed. The downflow is reduced, however, most of the flow still goes through the right section of the mold.

The time-averaged temperature distribution for the different scenarios is analyzed in **Figure 11**. To start with the non-clogged cases in Figure 11a,b, the obvious effect of the EMBr concludes in maintaining the superheat in the upper region of the mold close to the meniscus. That is a preferable consequence, providing sufficient flux melting, promoting the liquid slag infiltration, and resulting in the uniform solidification and better surface quality.

In the case of the clogged SEN in Figure 11c, the superheat is significantly low in the mold region, resulting in the undesired cold meniscus. Moreover, the hot jet on the non-clogged side causes the local shell remelting (see Figure 9b) close to the mold's exit, increasing the breakout risks.

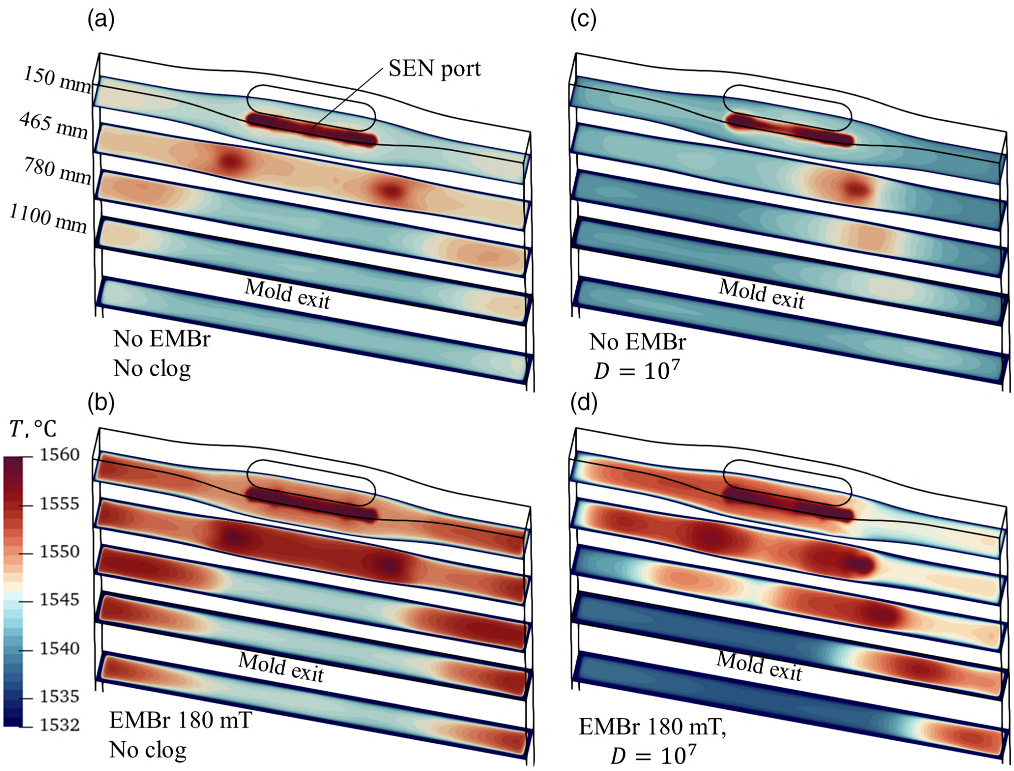

Figure 11. Time-averaged temperature field in the mold region. Cases without clogging: a) without and b) with the EMBr. Cases with the partially clogged SEN: c) no magnetic field; d) with the applied EMBr of 180 mT.

Even though the application of EMBr could not adjust the flow till a fully symmetric pattern (Figure 10b,d), it significantly improved the superheat distribution (Figure 11d) in comparison to the case in Figure 11c without magnetic field. The solid shell remelting region, outlined by the red dashed lines in Figure 9b, was diminished. Furthermore, when the EMBr is used, the shell profiles become more uniform in the transversal direction along the wide face (Figure 9c), especially at the mold's exit. It is worth mentioning that the flow asymmetry still causes shell thinning on the right narrow side. However, that emerges deeper in the strand region (see a white arrow marking in Figure 9c), where the thicker shell is already developed.

Since the discussed physical processes are of a strongly unsteady origin, the authors highly encourage the readers to watch the provided supplementary videos for the presented study, which reveal the transient dynamics of the described phenomena.

4. Conclusion

In the presented study, an asymmetric melt feeding through the thin-slab SEN was numerically investigated by applying partial blockage of the nozzle bore. The influence on the mold flow pattern and on the solid shell formation was considered without and with the applied EMBr magnetic field.

A strong melt flow disturbance between the clogged and the non-clogged side of the mold was observed. In the case without magnetic field, the jet oscillations between the narrow walls were detected. They lead to the partial shell remelting. Application of the EMBr stabilized the non-clogged side jet. However, that consequently causes stronger shell remelting at the strand region on the narrow side of the mold.

The variation of the porous resistance D for the clogged region between 10^6 and $10^8\,\mathrm{m}^{-2}$ was done considering the EMBr: 1) at the low D values, the flow asymmetry and the shell remelting are insignificant; 2) in the case of the strong porous resistance, the clogged side becomes completely blocked, and the downward jet on the opposite side causes pronounced shell thinning. However, the applied magnetic field maintains better superheat distribution in the upper mold region even for a very asymmetric scenario.

Current work considers a fixed-type EMBr arrangement for the conventionally symmetric flow. According to the numerical results, the applied magnetic field "freezes" the asymmetry and, thereby, enhances the solid shell remelting. However, the simulated equipment has adjustable cores, as many modern EMBr/EMS devices nowadays, which are dynamically operated. Thereby, prevention of the asymmetric flow pattern using the variably applied magnetic field is a topic for future studies.

Acknowledgements

The authors acknowledge the financial support by the Austrian Federal Ministry of Economy, Family and Youth and the National Foundation for Research, Technology and Development within the framework of the Christian Doppler Laboratory for Metallurgical Applications of Magnetohydrodynamics.

Conflict of Interest

The authors declare no conflict of interest.

Data Availability Statement

The data that support the findings of this study are available in the supplementary material of this article.

Keywords

asymmetric flows, continuous casting, electromagnetic brake, magnetohydrodynamics, OpenFOAM, thin slab

Received: January 31, 2022
Revised: March 29, 2022
Published online:

[1] C. Klinkenberg, B. Kintscher, K. Hoen, M. Reifferscheid, *Steel Res. Int.* **2017**, *88*, 1700272.
[2] P. D. Lee, P. E. Ramirez-Lopez, K. C. Mills, B. Santillana, *Ironmak. Steelmak.* **2012**, *39*, 244.
[3] K. C. Mills, P. Ramirez-Lopez, P. D. Lee, B. Santillana, B. G. Thomas, R. Morales, *Ironmak. Steelmak.* **2014**, *41*, 242.
[4] B. G. Thomas, *Steel Res. Int.* **2018**, *89*, 1700312.
[5] M. Vynnycky, *Metals* **2018**, *8*, 928.
[6] S.-M. Cho, M. Liang, H. Olia, L. Das, B. G. Thomas, in *TMS 2020 149th Annual Meeting & Exhibition Supplemental Proceedings, The Minerals, Metals & Materials Society, Ed., The Minerals, Metals & Materials Series* Springer International Publishing, Cham, **2020**, pp. 1161–1173.
[7] H. Barati, M. Wu, A. Kharicha, A. Ludwig, *Powder Technol.* **2018**, *329*, 181.
[8] H. Barati, M. Wu, A. Kharicha, A. Ludwig, *Metall. Mater. Trans. B* **2019**, *50*, 1428.
[9] H. Barati, M. Wu, A. Kharicha, A. Ludwig, *Steel Res. Int.* **2020**, *91*, 2000230.
[10] H. Barati, M. Wu, S. Michelic, S. Ilie, A. Kharicha, A. Ludwig, Y.-B. Kang, *Metall. Mater. Trans. B* **2021**.
[11] A. Vakhrushev, A. Kharicha, M. Wu, A. Ludwig, Y. Tang, G. Hackl, G. Nitzl, J. Watzinger, J. Bohacek, *Metals* **2021**, *11*, 1375.
[12] D. Gupta, A. K. Lahiri, *Steel Res.* **1992**, *63*, 201.
[13] D. Gupta, A. K. Lahiri, *Metall. Mater. Trans. B* **1996**, *27*, 757.
[14] E. Torres-Alonso, R. D. Morales, L. G. Demedices, A. Nájera, J. Palafox-Ramos, P. Ramirez-Lopez, *ISIJ Int.* **2007**, *47*, 679.
[15] H. Shen, B. Shen, B. Liu, *Steel Res. Int.* **2007**, *78*, 531.
[16] E. Torres-Alonso, R. D. Morales, J. Palafox-Ramos, P. Ramírez-López, *Steel Res. Int.* **2008**, *79*, 553.
[17] K. Timmel, T. Wondrak, M. Röder, F. Stefani, S. Eckert, G. Gerbeth, *Steel Res. Int.* **2014**, *85*, 1283.
[18] T. Wondrak, S. Eckert, G. Gerbeth, F. Stefani, K. Timmel, A. J. Peyton, N. Terzija, W. Yin, *Steel Res. Int.* **2014**, *85*, 1266.
[19] H. Zhou, L. Zhang, Q. Zhou, W. Chen, R. Jiang, K. Yin, W. Yang, *Steel Res. Int.* **2021**, *92*, 2000547.
[20] M. Wu, A. Vakhrushev, A. Ludwig, A. Kharicha, *IOP Conf. Ser.: Mater. Sci. Eng.* **2016**, *117*, 012045.
[21] B. G. Thomas, S. M. Cho, *IOP Conf. Ser.: Mater. Sci. Eng.* **2018**, *424*, 012027.
[22] S.-M. Cho, B. G. Thomas, *JOM* **2020**, *72*, 3610.
[23] Y. Yin, J. Zhang, H. Ma, Q. Zhou, *Steel Res. Int.* **2021**, *92*, 2000582.
[24] C. Wang, Z. Liu, B. Li, *Metals* **2021**, *11*, 948.

[25] Z. Li, L. Zhang, Y. Bao, D. Ma, E. Wang, *Metall. Mater. Trans. B* **2022**.
[26] O. Pütz, S. Rödl, *Steel Res. Int.* **2003**, *74*, 104.
[27] R. Liu, K. Blazek, B. Forman, C. Fritz, C. Graham, *Steel Res. Int.* **2019**, *90*, 1800398.
[28] B. Li, H. Lu, Y. Zhong, Z. Ren, Z. Lei, *Metals* **2019**, *9*, 1288.
[29] M. Sedén, B. Rydholm, *IOP Conf. Ser.: Mater. Sci. Eng.* **2019**, *529*, 012068.
[30] A. Vakhrushev, M. Wu, A. Ludwig, Y. Tang, G. Hackl, G. Nitzl, *Metall. Mater. Trans. B* **2014**, *45*, 1024.
[31] Z. Liu, A. Vakhrushev, M. Wu, E. Karimi-Sibaki, A. Kharicha, A. Ludwig, B. Li, *Metals* **2018**, *8*, 609.
[32] A. Vakhrushev, A. Kharicha, Z. Liu, M. Wu, A. Ludwig, G. Nitzl, Y. Tang, G. Hackl, J. Watzinger, *Metall. Mater. Trans. B* **2020**, *51*, 2811.
[33] A. Vakhrushev, A. Kharicha, E. Karimi-Sibaki, M. Wu, A. Ludwig, G. Nitzl, Y. Tang, G. Hackl, J. Watzinger, S. Eckert, *Metall. Mater. Trans. B* **2021**, *52*, 3193.
[34] H. G. Weller, G. Tabor, H. Jasak, C. Fureby, *Comput. Phys.* **1998**, *12*, 620.
[35] F. Nicoud, F. Ducros, *Flow Turbul. Combust.* **1999**, *62*, 183.
[36] P. A. Davidson, in *An Introduction To Magnetohydrodynamics*, 1st ed., Cambridge University Press, Cambridge, UK **2001**.
[37] W. S. Slaughter, in *The Linearized Theory Of Elasticity*, Birkhäuser Boston, Boston, MA, **2002**.
[38] A. Vakhrushev, M. Wu, A. Ludwig, Y. Tang, G. Hackl, G. Nitzl, *IOP Conf. Ser.: Mater. Sci. Eng.* **2012**, *33*, 012014.
[39] H. Liu, C. Yang, H. Zhang, Q. Zhai, Y. Gan, *ISIJ Int.* **2011**, *51*, 392.
[40] A. Vakhrushev, A. Kharicha, M. Wu, A. Ludwig, G. Nitzl, Y. Tang, G. Hackl, J. Watzinger, C. M. G. Rodrigues, *J. Iron Steel Res. Int.* **2022**, *29*, 88.
[41] J. Miettinen, S. Louhenkilpi, V.-V. Visuri, T. Fabritius, *IOP Conf. Ser.: Mater. Sci. Eng.* **2019**, *529*, 012063.
[42] B. G. Thomas, R. Singh, S. P. Vanka, K. Timmel, S. Eckert, G. Gerbeth, *J. Manufact. Sci. Product.* **2015**, *15*, 93.
[43] J. Bohacek, J. Kominek, A. Vakhrushev, E. Karimi-Sibaki, T. -W. Lee, *OpenFOAM J.* **2021**, *1*, 27.
[44] A. Kharicha, A. Vakhrushev, E. Karimi-Sibaki, M. Wu, A. Ludwig, *Phys. Rev. Fluids* **2021**, *6*, 123701.